## EDGE ARTICLE

Check for updates

All publication charges for this article
have been paid for by the Royal Society
of Chemistry

# Accelerating $N_2H_{4(ads)}$ formation by frustrated Lewis pairs in an oxyhydroxide for electrocatalytic ammonia oxidation into $N_2$

Meng-Ying Yin,[ab] Xing-Yuan Xia,[ab] Ting Dai,[ab] Xia Chen,[ab] Qiu-Ju Xing,[ab] Lei Tian[*abc] and Jian-Ping Zou [ID] [*ab]

Conventional catalysts based on the individual Oswin and Salomon (O–S) or Gerischer and Mauerer (G–M) mechanism cannot achieve direct electrocatalytic ammonia ($NH_3$) oxidation into nitrogen ($N_2$) with high activity and selectivity. Herein, a bimetallic nickel–cobalt oxyhydroxide ($Ni_{0.5}$–$Co_{0.5}$-OOH) with frustrated Lewis pairs was developed through an elaborate analysis of the binding types of $NH_3$ with the metal-oxide anode, efficiently integrating O–S and G–M mechanisms for converting $NH_3$ into $N_2$ with high activity (94%) and selectivity (63%), which is much superior to the anodes in the previous reports. The evidence of batch experiments, *in situ* characterization, and theoretical calculations confirms that two $NH_3$ molecules bind to $Co^{3+}$ sites (Lewis acid) in CoOOH and hydroxy sites (Lewis base) in NiOOH, respectively. Then, the $NH_{2(ads)}$ generated on the Lewis acid sites can quickly recombine with the $NH_{2(ads)}$ desorbed from the Lewis base sites, accelerating the formation of $N_2H_{4(ads)}$ and preventing the peroxidation of $NH_3$. The electrocatalytic system assembled with the $Ni_{0.5}$–$Co_{0.5}$-OOH anode shows excellent performance for $NH_3$ elimination in the secondary aerobic process effluent. Our work provides precious guidance for the design of novel anodes and sheds light on further promoting the performance of ammonia conversion.

## Introduction

The electrocatalytic ammonia oxidation reaction (EAOR) is viewed as a promising conversion measure due to its ability to address the growing problem of ammonia-containing wastewater pollution.[1–4] Nitrate and nitrite are the common products during the EAOR process, which could exacerbate secondary pollution.[5–7] As a comparison, nitrogen ($N_2$) is the most desirable product of the EAOR.[8–11] Therefore, it is urgent to exploit effective strategies to efficiently convert ammonia into $N_2$.

Direct electrocatalytic oxidation, based on anodic electron transfer, has been widely applied to ammonia pollution purification.[12–14] It is more environmentally friendly than indirect oxidation, which is related to the electrochlorination process because there are no toxic secondary products (chlorine gas and chlorine-containing intermediates) produced.[15–17] Until now, two possible conversion paths of the EAOR by direct

electrocatalytic oxidation have been proposed. One of them is the Oswin and Salomon (O–S) mechanism,[18] in which the adsorbed $NH_3$ dehydrogenates to $N_{(ads)}$ step by step and then converts into $N_2$ after the recombination of $N_{(ads)}$ (eqn (1)–(5)). During this process, the active sites in the anode have high Lewis acidity and mainly bind to the N atom in $NH_3$, ensuring strong binding energy for subsequent dehydrogenation. Unfortunately, excessive binding prevents the generated $N_{(ads)}$ from recombining, making it highly susceptible to peroxidation to generate $NO_2^-$ and $NO_3^-$.[19–21] The O–S mechanism demonstrates strong activity for the EAOR but extremely low selectivity for $N_2$ generation. The other reaction path for the EAOR is the Gerischer and Mauerer (G–M) mechanism,[22,23] in which the formation of $N_2$ is derived from the recombination of $N_xH_{y(ads)}$ intermediates (eqn (1)–(3) and (6)). The G–M mechanism shows a higher selectivity for $N_2$ formation than the O–S mechanism because the anodic active sites have high Lewis basicity and mainly bind to the H atom in $NH_3$, which is easily desorbed from the anodic surface after dehydrogenation, further efficiently converting into $N_2$. However, the binding energy is relatively weak when the active site binds to the H atom in $NH_3$, resulting in low efficiency of $NH_3$ dehydrogenation to $NH_{2(ads)}$ and sluggish EAOR kinetics.[24,25] The anode materials reported so far do not exhibit simultaneously high selectivity and high activity of the EAOR. Therefore, it is necessary to develop novel
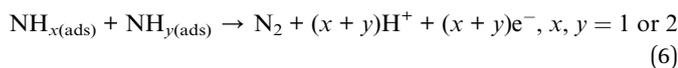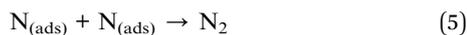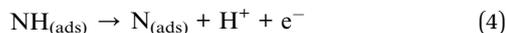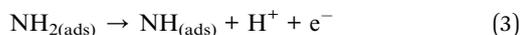
*[a]Key Laboratory of Jiangxi Province for Persistent Pollutants Prevention Control and Resource Reuse, Nanchang Hangkong University, Nanchang 330063, P. R. China*

*[b]National-Local Joint Engineering Research Center of Heavy Metals Pollutants Control and Resource Utilization, Nanchang Hangkong University, Nanchang 330063, P. R. China. E-mail: zjp_112@126.com*

*[c]School of Chemistry and Chemical Engineering, Institute of Clean Energy and Materials, Guangzhou Key Laboratory for Clean Energy and Materials, Key Laboratory for Water Quality and Conservation of the Pearl River Delta, Ministry of Education, Guangzhou University, Guangzhou 510006, P. R. China*

anode materials to realize the highly efficient and selective conversion of $NH_3$ into $N_2$ through direct oxidation.

$$NH_{3(aq)} \rightarrow NH_{3(ads)} \tag{1}$$

$$NH_{3(ads)} \rightarrow NH_{2(ads)} + H^+ + e^- \tag{2}$$

$$NH_{2(ads)} \rightarrow NH_{(ads)} + H^+ + e^- \tag{3}$$

$$NH_{(ads)} \rightarrow N_{(ads)} + H^+ + e^- \tag{4}$$

$$N_{(ads)} + N_{(ads)} \rightarrow N_2 \tag{5}$$

$$NH_{x(ads)} + NH_{y(ads)} \rightarrow N_2 + (x+y)H^+ + (x+y)e^-, x, y = 1 \text{ or } 2 \tag{6}$$

Inspired by the above mechanisms, it is found that the dehydrogenation of $NH_3$ into $NH_{2(ads)}$ is the rate-limiting step of the EAOR, while the recombination of $NH_{x(ads)}$ and $NH_{y(ads)}$ is the determining step for the selectivity of $N_2$ generation.[26] Theoretically, if the dehydrogenation in the O–S mechanism and the recombination of $NH_{x(ads)}$ and $NH_{y(ads)}$ in the G–M mechanism can be integrated together, the oxidation of $NH_3$ into $N_2$ can be effectively achieved with high activity and selectivity. Among the numerous anode materials,[27–30] metal oxyhydroxides (MOOH) are the desired anode materials for the efficient and selective conversion of $NH_3$ into $N_2$ due to the presence of frustrated Lewis pairs.[31,32] In detail, the metal atoms as Lewis acid sites can preferentially bind to the N atom due to the strong interaction between empty d-orbitals and lone pair electrons in the N atom, while the oxygen-containing functional groups as Lewis base sites can bind to the H atom (O–H–N) through hydrogen bonding. $NH_{x(ads)}$ generated on the Lewis acid sites will quickly recombine with $NH_{y(ads)}$ desorbed from the Lewis base sites, which can prevent the peroxidation of $NH_3$, thereby promoting EAOR efficiency and $N_2$ generation selectivity. More importantly, the presence of surface hydroxy groups enables oxyhydroxides to effectively resist the erosion of $Cl^-$, thereby demonstrating high reliability in actual wastewater treatment. Although a small number of hydroxyl oxide electrodes (NiOOH or FeOOH) have been reported for use in the EAOR process, the activity of the EAOR and the selectivity for $N_2$ generation are poor (below 30%).[33,34] Therefore, it is urgent to clarify the conversion law of $NH_3$ on different oxyhydroxides and develop highly active and selective oxyhydroxide anodes to achieve the EAOR.

Herein, a series of mono-metallic oxyhydroxide electrodes (MOOH, M: Mn, Co, Fe, Cu, Ni, and Zn) were synthesized, and their activity and selectivity of $N_2$ formation in the EAOR were investigated. Combined with the electronic structure of different transition metal ions, the transformation law between $NH_3$ and the active sites with different Lewis acidity/basicity was summarized. Based on this, a bimetallic oxyhydroxide was designed and synthesized, which can bind to the N and H atoms in $NH_3$, respectively, integrating the O–S and the G–M mechanisms together, further enhancing the EAOR efficiency and the selectivity of $N_2$ formation. The synergistic effect of the bimetallic oxyhydroxide was explored by batch performance

evaluation and structural characterization. Moreover, through XPS, in situ diffuse reflectance infrared Fourier transform spectroscopy (DRIFTS), and theoretical calculations, the conversion mechanism of $NH_3$ mediated by the bimetallic oxyhydroxide was further demonstrated. This work provides a new avenue for the design of anodic materials for the EAOR, which is in favor of the technological development of ammonia pollution purification.

## Materials and methods

### Materials and characterization

All chemicals were commercially obtained and used without further purification and the detailed information of materials is shown in Text S1 in the SI. The results of electrochemical analysis and characterization for catalyst structure and morphology are displayed in Text S2 in the SI. The evolution of conversion performance is displayed in Text S3 in the SI. The analytical methods for electrochemical characterization are displayed in Text S4 in the SI.

### Preparation of the anodes

Nickel foam (NF) was first cleaned through sonicating consecutively in acetone, 3 M HCl, ethanol, and deionized water for 15 min to remove the oxide layer and degrease the surface of the NF. Then, the treated NF was directly used as the substrate to deposit Ni–Co precursors. In a typical procedure of Ni–Co precursor fabrication, 2.0 mmol (582.06 mg) of $Co(NO_3)_2 \cdot 6H_2O$, 2.0 mmol (497.68 mg) of $Ni(CH_3COO)_2 \cdot 4H_2O$, 3.75 mmol (138.8 mg) of $NH_4F$ and 15 mmol (900.7 mg) of $CO(NH_2)_2$ were well dissolved in 50 mL of deionized water to form a mixture solution. The obtained solution was transferred into a 100 mL Teflon-lined stainless-steel autoclave. After immersing the washed NF ($1.5 \times 4$ cm$^2$) substrate in the homogeneous solution, the autoclave was sealed and heated at 90 °C for 7 h. After the autoclave cooled down to room temperature, the Ni–Co precursor loaded NF was taken out from the autoclave and rinsed with ultrapure water several times. The black electrode of Ni–Co oxyhydroxide was obtained by immersing the precursors in 5% NaClO solution as an oxidant for 30 min. The chemical oxidation of the precursors was carried out at pH 3–4 adjusted with $H_2SO_4$ or NaOH.

### Catalytic experiments

The initial concentration of ammonia was 20 mg N L$^{-1}$ and 50 mM $Na_2SO_4$ electrolyte was added into a 100 mL undivided cylindrical glass electrolytic cell. The different anodes and the Pt cathode were fixed at a gap of 1 cm in the reactor and connected to a potentiostat (CHI 660E electrochemical workstation (Shanghai, Chenhua, China)). Ag/AgCl was used as the reference electrode. The immersed area of the electrode was 4.5 cm$^2$. During the reaction process, the samples were taken with syringes at designated time intervals and immediately filtered through 0.45 μm polytetrafluoroethylene (PTFE) membranes. All experiments were conducted three times.

## Analysis methods

The concentration of ammonia was measured by Nessler's reagent colorimetric method. The samples were distilled first and the absorbance was obtained from a UV-vis spectrophotometer (UV-9000S, Metash Instruments Ltd, China) at the wavelength of 420 nm.[35] The concentrations of nitrate ($NO_3^-$) and nitrite ($NO_2^-$) were determined by the ultraviolet spectrophotometry and N-(1-naphthyl)-ethylenediamine dihydrochloride spectrophotometric method, respectively.[36] The concentration of total nitrogen (TN) was measured by the traditional alkaline persulfate oxidation method.[37] The pH value was measured with a pH meter (Mettler Toledo-FE28, Swit). The ammonia removal ($R$) and selectivity of nitrogen conversion ($S_N$) were calculated using equations below:

$$R = \frac{[NH_3]_0 - [NH_3]_t}{[NH_3]_0} \times 100\% \tag{7}$$

$$S_N = \frac{[N]_t}{[NH_3]_0 - [NH_3]_t} \times 100\% \tag{8}$$

where [N] denotes the concentration of nitrogen products, including [$NO_2^-$–N], [$NO_3^-$–N] and [$N_2$–N].

Current efficiency is expressed as eqn (9):

$$CE\ (\%) = \frac{n_i \times F \times (C_0 - C_t) \times V}{M \times \int_0^t IA dt} \times 100\% \tag{9}$$

Here, $C_0$ is the initial concentration of $NH_3$–N, $C_t$ is the concentration of $NH_3$–N at degradation time $t$ (s), $V$ is the volume of the electrolyte (0.1 L), $M$ is the molar mass of $NH_3$–N (14 g mol$^{-1}$), $I$ is the current density (A m$^{-2}$), $A$ is the effective area of the electrodes (4.5 m$^{-2}$), $F$ is the Faraday constant (96 485.3 C mol$^{-1}$) and $n$ is the number of electrons needed for the oxidation of one mole of ammonia ($n = 3$).
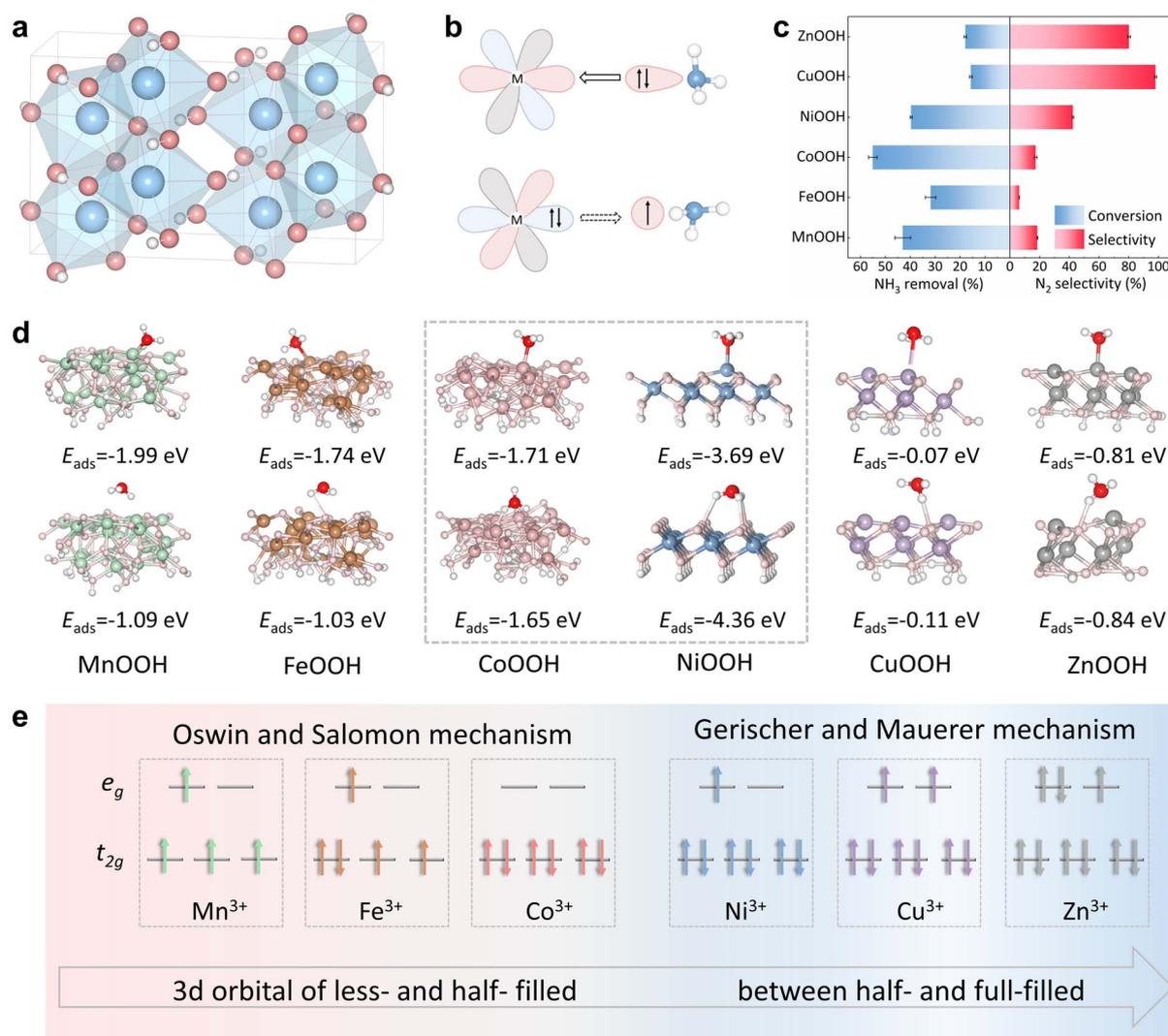


Fig. 1 (a) Crystal structure of MOOH; (b) different adsorption types with $NH_3$; (c) EAOR activity and selectivity of MOOH with different transition metal ions ($E$ = 1.8 V, pH = 11, 0.05 M Na$_2$SO$_4$); (d) calculated adsorption energies of ammonia molecules at metal and hydroxyl sites in monometallic oxyhydroxides; (e) diagram of d orbital electron configuration of different transition metal ions.

The energy consumption (EC, kWh m$^3$) was calculated through eqn (10).

$$EC = \frac{U \times I \times t \times 1000}{\log(C_0/C_t) \times V} \tag{10}$$

where $U$ is the applied voltage (V), $I$ is the average current (A), $t$ is the time (h), $V$ is the solution volume (L), and $\log(C_0/C_t)$ is the logarithm of the initial and instant concentrations of the ammonia.

### Theoretical calculation

The present first principle DFT calculations are performed with the Vienna *Ab initio* Simulation Package (VASP) with the projector augmented wave (PAW) method. Detailed information about the calculation procedure is provided in Text S5 in the SI.

## Results and discussion

### Lewis acidity/basicity on NH$_3$ conversion

The structure characterization studies of different MOOH are shown in Fig. S1 and S2. The prototypical MOOH oxyhydroxide has a typical cubic crystal structure. Metal atoms are located at the centre of $MO_6$ octahedra and the layers are linked by

hydrogen bonds (Fig. 1a). When there are many unoccupied d orbitals, metal atoms in MOOH can bind with N atoms in NH$_3$ during the adsorption process.[38] In contrast, the O atoms in MOOH may bind with H in NH$_3$ through a hydrogen bond (Fig. 1b).[39] With the outer 3d orbitals being gradually filled by electrons, the Lewis acidity of metal sites decreases and the Lewis basicity of hydroxy sites increases (Fig. 1c, e and S3). The EAOR performance of MOOH (from Mn$^{3+}$ to Zn$^{3+}$) increases first and then decreases (CoOOH > MnOOH > NiOOH > FeOOH > ZnOOH > CuOOH). When the d orbitals of the metal atom in MOOH are before half-filled, the adsorption energies of NH$_3$ at the metal sites are higher than those at the hydroxy sites (Fig. 1d), which can strongly bind with the N atom in NH$_3$, thus giving it strong EAOR performance. However, the overly strong force leads to the peroxidation of NH$_{x(ads)}$ intermediates into NO$_2^-$/NO$_3^-$, which follows the typical O–S mechanism and exhibits low N$_2$ formation selectivity. As a comparison, after the d orbital is half-filled, NH$_3$ adsorbs more strongly at the hydroxy sites than at the metal sites. Though the EAOR performance of MOOH is relatively sluggish, the N$_2$ formation selectivity is dramatically increased, which can be attributed to the change of the catalytic mechanism from O–S to G–M. In the two stages before and after a half-filled electronic orbital, CoOOH and
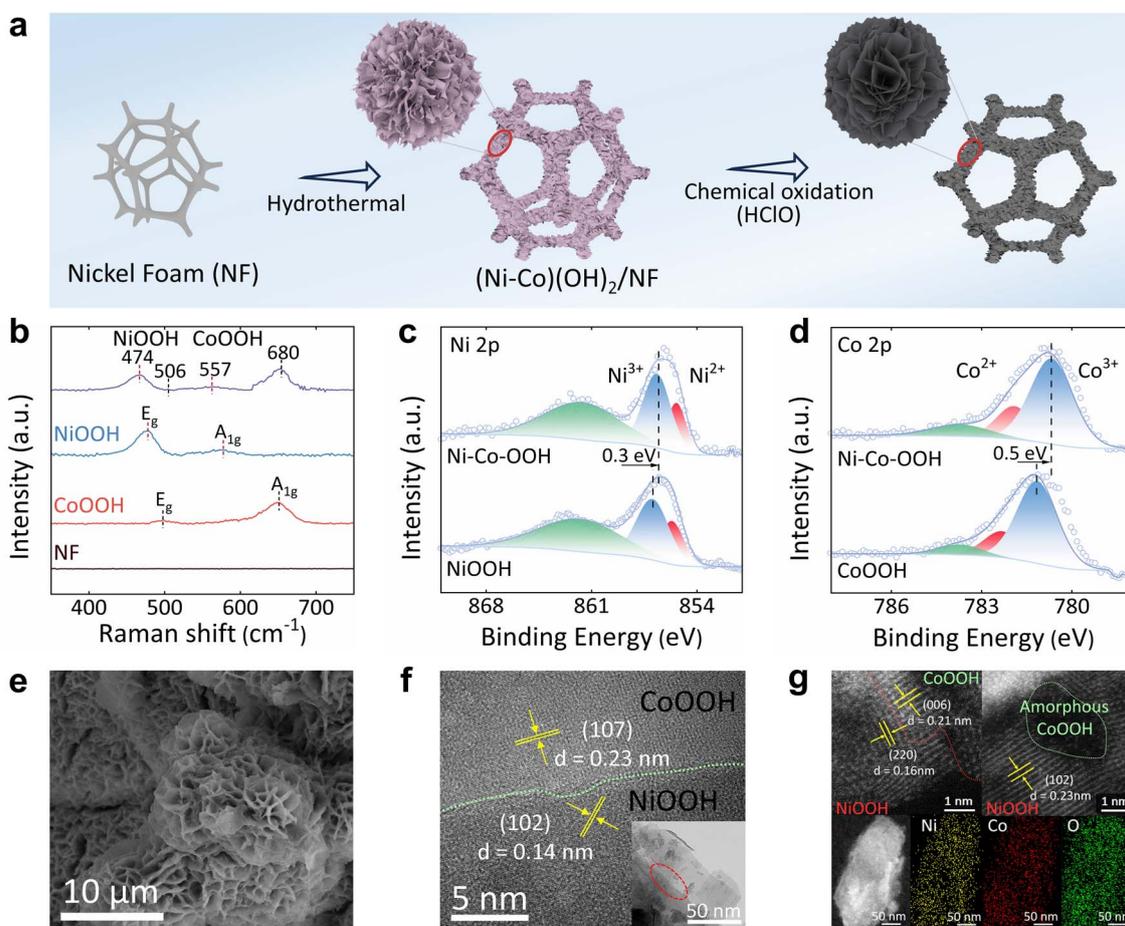


Fig. 2 (a) Synthesis diagram of Ni–Co-OOH; (b) Raman spectra of Ni–Co-OOH, CoOOH and NiOOH and nickel foam (NF); (c) Ni 2p XPS of Ni–Co-OOH and NiOOH; (d) Co 2p XPS of Ni–Co-OOH and CoOOH; (e) SEM images of Ni–Co-OOH; (f) TEM images of Ni–CoOOH; (g) HAADF-STEM image of Ni–Co-OOH.

NiOOH exhibited optimal Lewis acidity/basicity and superior activity and selectivity for the EAOR compared to other MOOH or bimetallic systems (Fig. S4), respectively. Hence, Co and Ni elements were used to assemble the subsequent bimetallic oxyhydroxide catalysts to integrate the O–S and G–M mechanisms on a catalyst.

## Synthesis and characterization of Ni–Co-OOH

The Ni–Co oxyhydroxide (Ni–Co-OOH) was synthesized following the schematic diagram in Fig. 2a. The XRD pattern of Ni–Co-OOH shows the presence of characteristic peaks attributed to NiOOH and CoOOH, respectively (Fig. S5). As shown in Fig. 2b, Raman spectra further demonstrate that the peaks located at 474 and 557 $cm^{-1}$ are attributed to the $E_g$ bending and $A_{1g}$ stretching vibrations of Ni–O of NiOOH, respectively, whereas the peaks observed at 506 and 680 $cm^{-1}$ are assigned to the CoOOH in Ni–Co-OOH.[40,41] The Raman spectra show a slight shift in the vibrational frequencies of Ni–O and Co–O bonds compared to NiOOH and CoOOH, indicating there is electronic interaction between NiOOH and CoOOH. Besides, X-ray photoelectron spectroscopy (XPS) shows that two peaks in Co $2p_{3/2}$ at 780.8 and 781.9 eV are assigned to $Co^{3+}$ and $Co^{2+}$,[42–44] respectively. For Ni $2p_{3/2}$ spectra, the peaks at 855.36 and 856.66 eV are attributable to the $Ni^{2+}$ and $Ni^{3+}$,[45–47] respectively (Fig. 2c and d). Ni/Co–O bonds are also identified by the characteristic peak at 529.7 eV from O 1s spectra (Fig. S6). The peaks of $Ni^{3+}$ and $Co^{3+}$ are observed to shift by 0.3 eV and 0.5 eV, respectively, towards a lower binding energy compared to their mono-metallic oxyhydroxide, proving the electron transfer from $Co^{3+}$ to $Ni^{3+}$. The coupling of $Ni^{3+}$ and $Co^{3+}$ via the bridging $O^{2-}$ facilitates π-donation from $O^{2-}$ to $Ni^{3+}$, resulting in the overall electron transfer from $Co^{3+}$ to $Ni^{3+}$, which is in agreement with the Raman spectra results. In addition, scanning electron microscopy (SEM) images show that the morphology of Ni–Co-OOH is a nanoplate structure covered with nano-flower spheres, where NiOOH and CoOOH are nanoplates and nano-flower spheres, respectively, confirming that Ni–Co-OOH is a composite and CoOOH is loaded on the surface of NiOOH (Fig. 2e, S7 and S8). A further inspection of these nanosheet structures with high-resolution TEM and spherical aberration-corrected high angle annular dark field scanning transmission electron microscopy (HAADF-STEM) was conducted. As shown in Fig. 2f and g, the images demonstrate the heterojunction region of Ni–Co-OOH, indicating that there are two different phases on both sides of the interface. The lattice distances are 1.6, 2.1 and 2.3 Å, which are consistent with the (2 2 0) facet of NiOOH, (0 0 6) facet of CoOOH and (1 0 2) facet of NiOOH, respectively. Therefore, the aforementioned characterization evidently confirms the successful preparation of the Ni–Co bimetallic oxyhydroxide catalyst by a two-stage method of hydrothermal and chemical oxidation and it is a biphasic composite with a heterojunction structure.

## EAOR activity, N₂ selectivity and practical application

The EAOR activity of CoOOH and NiOOH is 93.8% and 24.1%, whereas the selectivity of $N_2$ is 1.3% and 35.7% and the selectivity of $NO_3^-$ is 74% and 24%, respectively, which typically follows the O–S and G–M mechanisms, respectively (Fig. 3a). $Ni_x$–$Co_{1-x}$-OOH catalysts with different Ni/Co ratios were obtained by varying the precursor dosages based on the similar solubility products of $Ni(OH)_2$ and $Co(OH)_2$ ($k_{sp}(Ni(OH)_2) = 2 \times 10^{-15}$, $k_{sp}(Co(OH)_2) = 1.6 \times 10^{-15}$) (Table S1). $Ni_{0.5}$–$Co_{0.5}$-OOH (Ni : Co = 0.5 : 0.5) exhibits higher EAOR activity (94.0%) and $N_2$ formation selectivity (63.0%) than $Ni_{0.75}$–$Co_{0.25}$-OOH, $Ni_{0.25}$–$Co_{0.75}$-OOH and the physically mixed CoOOH/NiOOH, which is superior to the electrocatalysts reported in the previous literature (Fig. S9–S11 and Table S2).[48–54] Since the strong interaction between the Co-based Lewis acid sites and the N atom can cause difficulty in the desorption of N-containing intermediates from the anodic surface, the introduction of excessive CoOOH into NiOOH inhibits the formation of $N_2$, while generating more $NO_3^-$ during the EAOR process. In addition, as shown in Fig. 3b, the NiOOH anode shows low faradaic efficiency (7.5%) and high energy consumption (150 kWh kg $N^{-1}$) for $NH_3$ conversion. Conversely, the current efficiency of Co-based oxyhydroxides significantly improves to 20–40%, while the low $N_2$ selectivity makes the $NO_2^-$ and $NO_3^-$ predominate the energy consumption. The $Ni_{0.5}$–$Co_{0.5}$-OOH can reach the highest faradaic efficiency (42%) and the energy consumption reaches a minimum value of 26.3 kWh kg $N^{-1}$, which further verifies the superior activity of $Ni_{0.5}$–$Co_{0.5}$-OOH for the EAOR.

With the increase of applied voltage from 1.6 V to 2.1 V vs. RHE, the EAOR activity of $Ni_{0.5}$–$Co_{0.5}$-OOH increases, while the $N_2$ formation selectivity is optimal (63.0%) at 1.8 V (Fig. 3c and S12). When excessive voltage is applied, the anodic oxygen evolution reaction (OER) may be severe, and $NH_3$ can be easily peroxided into $NO_3^-$ and $NO_2^-$, resulting in a low $N_2$ formation selectivity. Besides, the removal of $NH_3$ and the formation selectivity of $N_2$ is significantly inhibited with increasing $NH_3$ concentrations (Fig. 3c and S13), which may be due to the saturation of the active sites on the electrode surface. In addition, the oxidation efficiency of $NH_3$ increases from 3.9% to 99.3%, whereas the $N_2$ formation selectivity declines from 100% to 38.4% with the increase in pH from 10 to 13 (Fig. 3c and S14). At a relatively low pH, $NH_3$ can be protonated into $NH_4^+$ ($pK_a(NH_4^+/NH_3) = 9.25$), leading to the sluggish anodic oxidation of $NH_4^+$ caused by electrostatic repulsion. In contrast, at a high pH, $N_2$ production selectivity is significantly inhibited due to the serious OER and $NH_3$ peroxidation (eqn (S4)–(S10)) at the anode, leading to the generation of $NO_2^-$ and $NO_3^-$. These results indicate that the best performance of the $Ni_{0.5}$–$Co_{0.5}$-OOH anode can be obtained when the voltage is 1.8 V, the $NH_3$ concentration is 20 mg $L^{-1}$ and the pH is 12.

To evaluate the practical application of the $Ni_{0.5}$–$Co_{0.5}$-OOH anode, ten cycles of experiments were carried out. As shown in Fig. 3d, the $NH_3$ conversion is around 90%, while the $N_2$ formation selectivity is still over 60% within 10 cycles, indicating that $Ni_{0.5}$–$Co_{0.5}$-OOH shows remarkable stability. Besides, there are no leaching concentrations of cobalt/nickel ions detected even in chloride-containing solutions and no change is observed in the metal value state and structure during ten cycles (Fig. S15–S18), which further confirms the stability of $Ni_{0.5}$–$Co_{0.5}$-OOH. Unlike the lattice oxygen mechanism involved

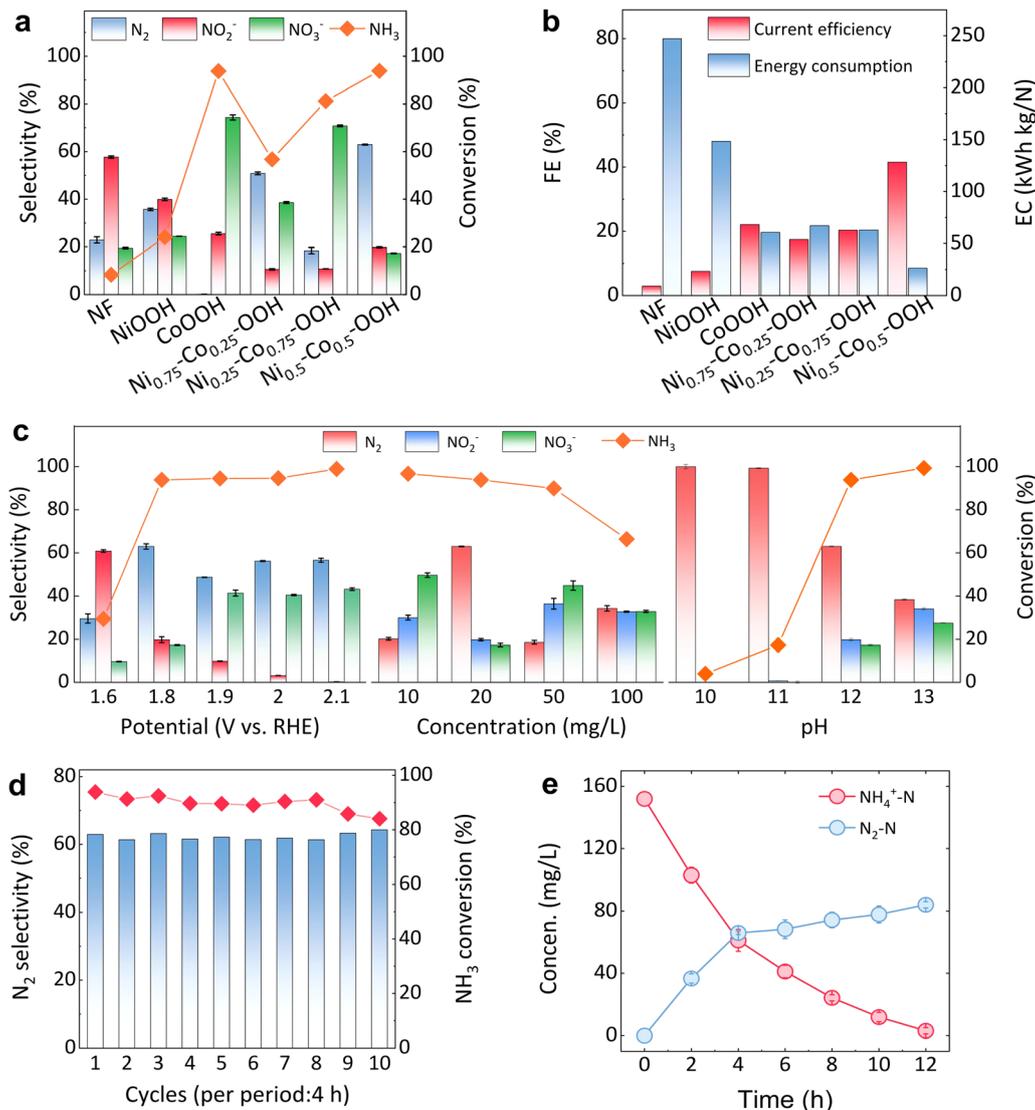Fig. 3 (a) EAOR activity and product selectivity with different anodes ($E$ = 1.8 V, pH = 12, 0.05 M $Na_2SO_4$); (b) Faradaic efficiency and energy consumption of the EAOR with different anodes ($E$ = 1.8 V, pH = 12, 0.05 M $Na_2SO_4$); (c) EAOR activity and product selectivity of $Ni_{0.5}$–$Co_{0.5}$-OOH under different conditions; (d) ten cycles of $Ni_{0.5}$–$Co_{0.5}$-OOH ($E$ = 1.8 V, pH = 12, 0.05 M $Na_2SO_4$); (e) EAOR activity of $Ni_{0.5}$–$Co_{0.5}$-OOH for practical wastewater ($E$ = 2.0 V, 0.05 M $Na_2SO_4$).

in the OER processes (Fig. S19), surface reconstruction does not occur during the EAOR process. In addition, the electrocatalytic system assembled with the $Ni_{0.5}$–$Co_{0.5}$-OOH anode was applied to treat the practical ammonia-containing wastewater, which was the secondary aerobic process effluent. As shown in Fig. 3e and S20, the $NH_3$ conversion is around 99%, while the $N_2$ formation selectivity (55%) is much greater than that of nitrate (31%) and nitrite (11%). In conclusion, the $Ni_{0.5}$–$Co_{0.5}$-OOH electrode has excellent stability and shows good application potential in the treatment of practical ammonia-containing wastewater.

### Electrochemical characterization

Diverse electrochemical characterization studies were performed to explore the EAOR activity of $Ni_{0.5}$–$Co_{0.5}$-OOH. As shown in the linear sweep cyclic voltammetry (LSV) and Tafel curves (Fig. 4a and S21–S23), a lower onset potential (1.28 V) and a lower Tafel slope (128 mV $dec^{-1}$) are observed in the presence of $NH_3$, demonstrating that $Ni_{0.5}$–$Co_{0.5}$-OOH is more susceptible to the EAOR than the OER (1.45 V, 244 mV $dec^{-1}$). Besides, the polarization current of $Ni_{0.5}$–$Co_{0.5}$-OOH in the presence of $NH_3$ is beyond that of CoOOH and the corresponding Tafel slope is the lowest derived from these catalysts, which further indicates exceptional activity of $Ni_{0.5}$–$Co_{0.5}$-OOH for the EAOR (Fig. 4b, S24 and S25). Moreover, the electrochemical surface area is calculated from the values of double layer capacitance ($C_{dl}$) to be 35.5, 31.75, 50.25, 38 and 69.5 $cm^2$ for NiOOH, CoOOH, $Ni_{0.75}$–$Co_{0.25}$-OOH, $Ni_{0.25}$–$Co_{0.75}$-OOH and $Ni_{0.5}$–$Co_{0.5}$-OOH, respectively (Fig. 4c and S26). This result confirms that there are more catalytically active sites on the $Ni_{0.5}$–$Co_{0.5}$-OOH
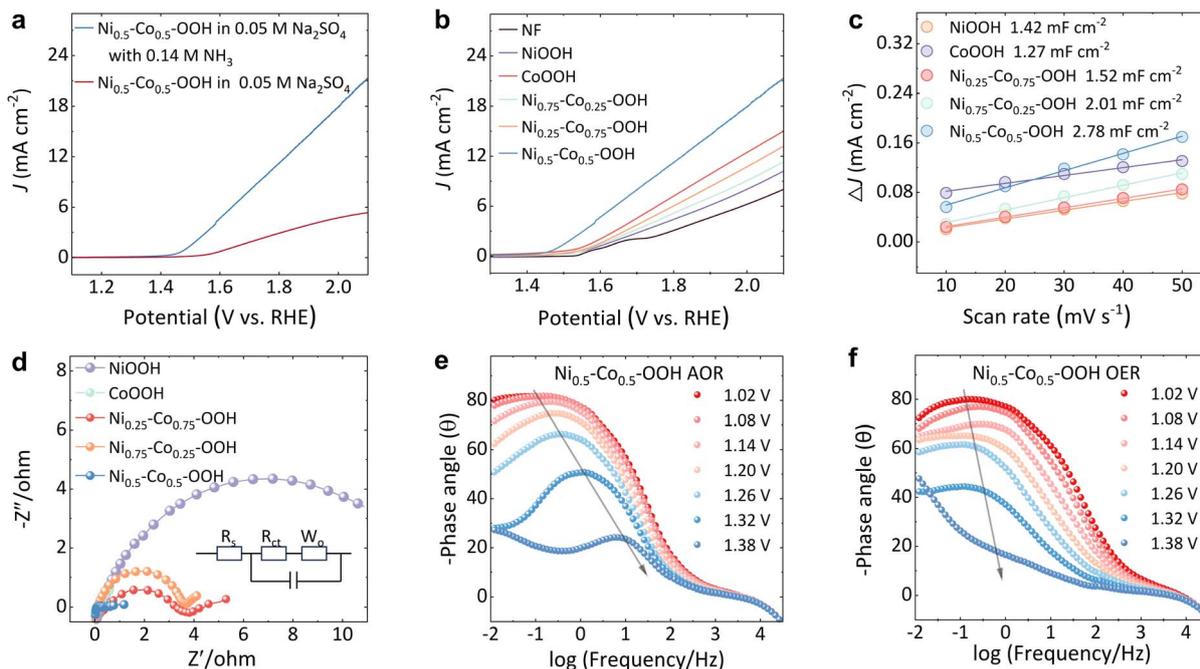
**Fig. 4** (a) LSV curves of $Ni_{0.5}-Co_{0.5}$-OOH with or without $NH_3$; (b) LSV curves of different oxyhydroxides in the presence of $NH_3$; (c) electrochemical double-layer capacitance ($C_{dl}$) of different oxyhydroxides; (d) electrochemical impedance spectroscopy of different oxyhydroxides, the inset is the equivalent circuit for EIS fitting; (e and f) Bode phase plots of $Ni_{0.5}-Co_{0.5}$-OOH for the EAOR and OER.

than other oxyhydroxides because of the synergistic effect of CoOOH and NiOOH. Furthermore, $Ni_{0.5}-Co_{0.5}$-OOH displays the smallest Nyquist semicircle diameter, suggesting the lowest charge transfer resistances (1.2 Ω) during the reaction process (Fig. 4d). Meanwhile, the *in situ* electrochemical impedance spectroscopy (EIS) tests were conducted to uncover the dynamic interfacial changes of the catalyst (Fig. 4e and f). It is observed that the phase angle of the HF region in the $NH_3$ solution sharply decreased from 1.26 V, indicating the fast charge-transfer kinetics of the EAOR. Thus, the $Ni_{0.5}-Co_{0.5}$-OOH/NF electrocatalyst exhibits extraordinary activity for the EAOR.

### Direct NH3 oxidation mechanism

XPS and *in situ* diffuse reflectance infrared Fourier transform spectroscopy (DRIFTS) were used to detect the variation of $Ni_{0.5}-Co_{0.5}$-OOH/NF and $NH_3$ molecules during the EAOR process. As shown in Fig. 5a and b, the proportions of $Ni^{3+}/Ni^{2+}$ and $Co^{3+}/Co^{2+}$ first decrease and then increase close to the initial value during the EAOR process (Tables S3 and S4). Regardless of O–S and G–M mechanisms, trivalent metal ions with high oxidative potential in oxyhydroxides act as the electron acceptors to induce the dehydrogenation of $NH_{3(ads)}$ into $NH_{2(ads)}$. As a result, the decrease of $Ni^{3+}$ and $Co^{3+}$ in $Ni_{0.5}-Co_{0.5}$-OOH occurs at the initial stage of the EAOR. Subsequently, the formed $Ni^{2+}$ and $Co^{2+}$ in $Ni_{0.5}-Co_{0.5}$-OOH can be further oxidized into $Ni^{3+}$ and $Co^{3+}$ through anodic electron transfer. Besides, it can be seen from the potential-dependent *in situ* DRIFTS that the peak around 1102 $cm^{-1}$ is ascribable to the symmetric N–H bending vibration, which stems from the $NH_{3(ads)}$ or $NH_{x(ads)}$ intermediates (Fig. 5c and S27). Notably, there is a new peak at

1244 $cm^{-1}$ with increasing potential, which is assigned to the stretching of $H_2N–NH_{2(ads)}$.[55,56] This phenomenon manifests that the formation of $N_2$ during the EAOR process is derived from the further conversion of $N_2H_{4(ads)}$. A negligible peak around 1605 $cm^{-1}$ in DRIFTS, corresponding to the N–O vibration, is also observed, resulting from a few $NO_2^-$ or $NO_3^-$ generated from the peroxidation of $NH_3$. In addition, as shown in Fig. 5d, *in situ* Raman spectra of CoOOH and NiOOH show an increasing intensity of Ni–OH and Co–N peaks, respectively, with the potential increasing from 1.2 V to 1.9 V *vs.* RHE. It is noted that the stretching vibrations of Co–N and Ni–OH bonds are observed in Ni–Co-OOH throughout the reaction, which serves to further verify the synergistic effect of the frustrated Lewis pairs. The intensity of the Ni–OH peak, which arises from strong hydrogen bonding between NiOOH and $NH_3$,[57–59] initially increases and then decreases as the potential is raised from 1.2 V to 1.9 V. This trend suggests that NiOOH undergoes reversible transformation to $Ni(OH)_2$ and eventually returns to its initial state, accompanied by the dehydrogenation of $NH_3$, formation of $N_2H_{4(ads)}$, and generation of $N_2$ on frustrated Lewis pairs. A similar reversible behavior is observed for CoOOH in the Ni–Co-OOH system. The change in Co–N strength also confirms that $Co^{3+}$ is the site for $NH_3$ oxidation. The frustrated Lewis acid–base pair composed of $Co^{3+}$ and hydroxy facilitates $N_2H_{4(ads)}$ formation, thus promoting the selective ammonia oxidation into $N_2$.

DFT calculations were performed to explore the conversion path of $NH_3$ mediated by $Ni_{0.5}-Co_{0.5}$-OOH. According to the structural characterization, the $Ni_{0.5}-Co_{0.5}$-OOH model with the heterojunction is simulated (Fig. S28). It is known that NiOOH following
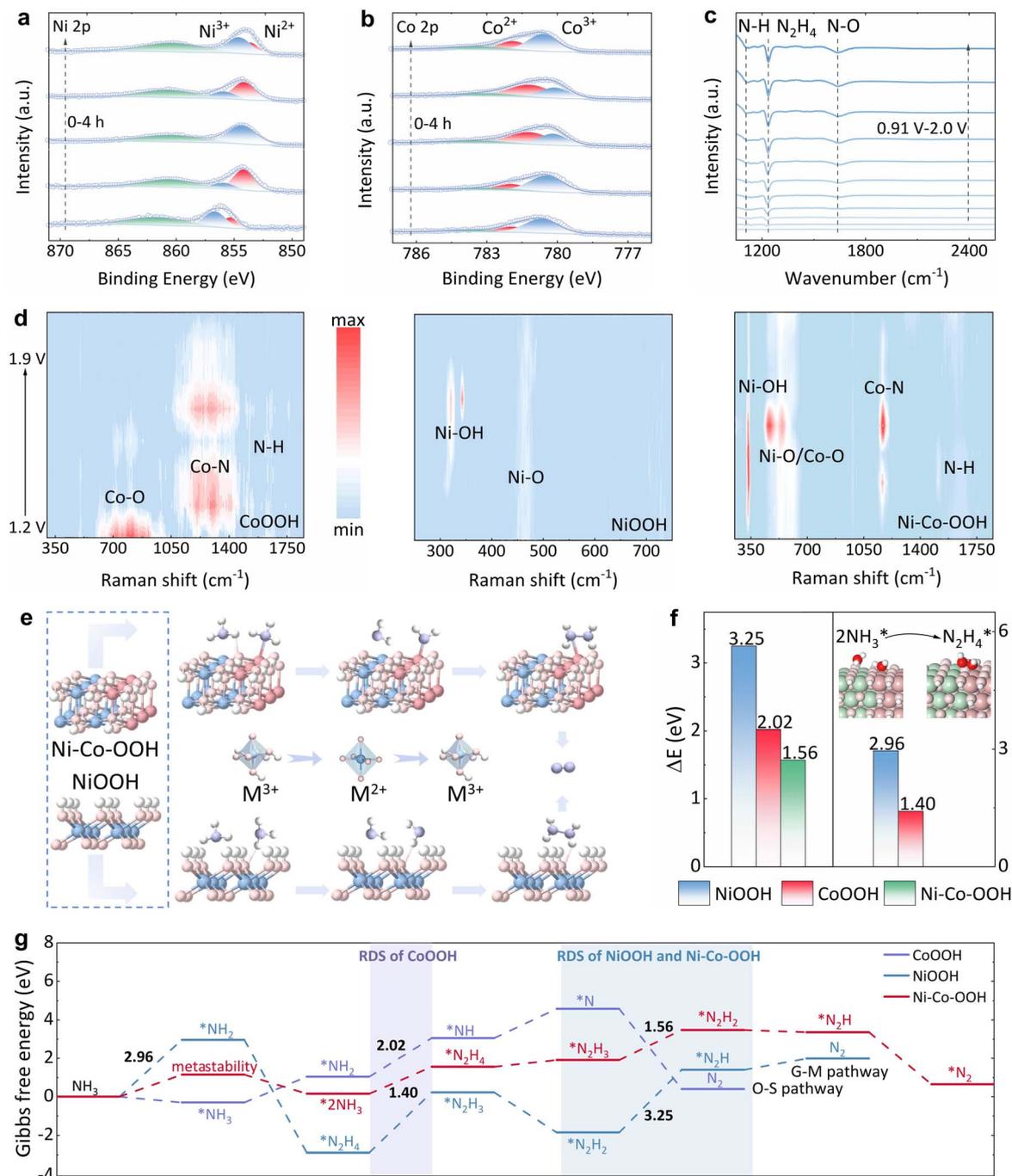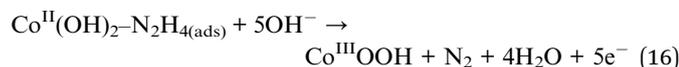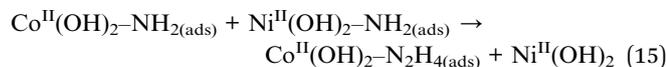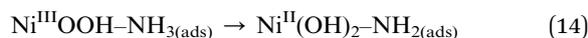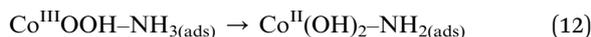
**Fig. 5** (a) Ni 2p XPS of the $Ni_{0.5}$–$Co_{0.5}$-OOH system within 4 h; (b) Co 2p XPS of the $Ni_{0.5}$–$Co_{0.5}$-OOH system; (c) *in situ* DRIFTS spectra of the $Ni_{0.5}$–$Co_{0.5}$-OOH system with applied potential positive scanning from 0.91 to 2.0 V *vs.* RHE; (d) *in situ* Raman test of CoOOH (left), NiOOH (middle) and $Ni_{0.5}$–$Co_{0.5}$-OOH (right) systems; (e) the modeled $N_2H_{4(ads)}$ formation pathway of the $Ni_{0.5}$–$Co_{0.5}$-OOH and NiOOH system, respectively; (f) the pivotal potential gaps of RDS and the formation step of $N_2H_{4(ads)}$ in Ni–Co-OOH, CoOOH and NiOOH systems; (g) Gibbs free energy diagrams of the EAOR by G–M and O–S mechanisms of the $Ni_{0.5}$–$Co_{0.5}$-OOH and CoOOH system, respectively.

the G–M mechanism exhibits high selectivity for $N_2$ generation, which is primarily derived from the conversion of $N_2H_{4(ads)}$ intermediates. The $N_2H_{4(ads)}$ generation energy barrier is compared to determine the $N_2$ generation selectivity of Ni–Co-OOH. As shown in Fig. 5e and f, for $Ni_{0.5}$–$Co_{0.5}$-OOH, two $NH_3$ molecules bind to $Co^{3+}$ sites and hydroxy sites (the adsorption model as displayed in

Fig. S29), which is the integration of O–S and G–M mechanisms. Then, the $NH_{2(ads)}$ generated on the $Co^{3+}$ sites can quickly recombine with the $NH_{2(ads)}$ desorbed from the hydroxy sites into $N_2H_{4(ads)}$ (eqn (11)–(16)). As a comparison, for NiOOH, the formation of $N_2H_{4(ads)}$ is derived from the recombination of two $NH_{2(ads)}$ at hydroxy sites. The lower free energy of the $N_2H_{4(ads)}$ formation

confirms that the $Ni_{0.5}$–$Co_{0.5}$-OOH anode exhibits a higher $N_2$ selectivity for the EAOR than NiOOH. In addition, the $NH_3$ conversion path is further analysed to explore the EAOR activity of the $Ni_{0.5}$–$Co_{0.5}$-OOH anode. As shown in Fig. 5f and g, after the formation of the $N_2H_{4(ads)}$ intermediate, its continuous dehydrogenation into $N_2$ occurs at $Co^{3+}$ sites. The rate-limiting step of the EAOR with the $Ni_{0.5}$–$Co_{0.5}$-OOH anode is the formation of $N_2H_{2(ads)}$ (1.56 eV), which is the lowest in comparison with the O–S mechanism of CoOOH (2.02 eV) and G–M mechanism of NiOOH (3.25 eV). This result further verifies that the EAOR activity of the $Ni_{0.5}$–$Co_{0.5}$-OOH anode is superior to that of CoOOH. In summary, due to the synergetic effect of the frustrated Lewis pairs in $Ni_{0.5}$–$Co_{0.5}$-OOH, the O–S and G–M mechanisms are integrated, and the recombination of $NH_{2(ads)}$ intermediates into $N_2H_{4(ads)}$ intermediates is facilitated, thereby immensely promoting the EAOR activity and $N_2$ formation selectivity.

$$Co^{III}OOH + NH_3 \rightarrow Co^{III}OOH–NH_{3(ads)} \quad (11)$$

$$Co^{III}OOH–NH_{3(ads)} \rightarrow Co^{II}(OH)_2–NH_{2(ads)} \quad (12)$$

$$Ni^{III}OOH + NH_3 \rightarrow Ni^{III}OOH–NH_{3(ads)} \quad (13)$$

$$Ni^{III}OOH–NH_{3(ads)} \rightarrow Ni^{II}(OH)_2–NH_{2(ads)} \quad (14)$$

$$Co^{II}(OH)_2–NH_{2(ads)} + Ni^{II}(OH)_2–NH_{2(ads)} \rightarrow \\ Co^{II}(OH)_2–N_2H_{4(ads)} + Ni^{II}(OH)_2 \quad (15)$$

$$Co^{II}(OH)_2–N_2H_{4(ads)} + 5OH^- \rightarrow \\ Co^{III}OOH + N_2 + 4H_2O + 5e^- \quad (16)$$

## Conclusions

In conclusion, this study developed a bimetallic nickel–cobalt oxyhydroxide (Ni–Co-OOH) to integrate O–S and G–M mechanisms together. The synergy of the frustrated Lewis acid–base pairs is utilized for the selective conversion of $NH_3$ into $N_2$. Noteworthily, two $NH_3$ molecules bind to $Co^{3+}$ sites (Lewis acid) in CoOOH and hydroxy sites (Lewis base) in NiOOH. Then, the $NH_{2(ads)}$ desorbed from the hydroxy sites can rapidly recombine with the $NH_{2(ads)}$ generated in $Co^{3+}$ into $N_2H_{4(ads)}$, leading to the formation of $N_2$. The Ni–Co-OOH anode exhibits excellent activity (94%) and selectivity (63%) for the EAOR beyond other catalysts. This work provides a new idea for designing and preparing novel catalysts to improve the performance of ammonia conversion technology.

## Author contributions

Meng-Ying Yin: writing – original draft, formal analysis, data curation, conceptualization. Xing-Yuan Xia: formal analysis, data curation. Ting Dai: formal analysis, data curation, software. Xia Chen: formal analysis, conceptualization, software. Qiu-Ju Xing: resources, supervision, visualization. Lei Tian: project administration, writing – review & editing, methodology. Jian-Ping Zou: writing – review & editing, methodology, resources, project administration, funding acquisition.

## Conflicts of interest

There are no conflicts to declare.

## Data availability

Data will be made available on request.

The general information, methods and supplementary data associated with this article are provided in the supplementary information (SI). See DOI: https://doi.org/10.1039/d5sc06524k.

## Acknowledgements

## Notes and references

1 M. E. Ahmed, M. R. Boroujeni, P. Ghosh, C. Greene, S. Kundu, J. A. Bertke and T. H. Warren, Electrocatalytic Ammonia Oxidation by a Low-Coordinate Copper Complex, *J. Am. Chem. Soc.*, 2022, **144**, 21136–21145.

2 T. Gupta, Sanyam, S. Saraswat, A. Mondal and B. Mondal, Electrochemical Ammonia Oxidation with a Homogeneous Molecular Redox Mediator, *Chem. Sci.*, 2025, **16**, 14377–14383.

3 Y. Chen, G. Zhang, Q. Ji, H. Lan, H. Liu and J. Qu, Visualization of Electrochemically Accessible Sites in Flow-through Mode for Maximizing Available Active Area toward Superior Electrocatalytic Ammonia Oxidation, *Environ. Sci. Technol.*, 2022, **56**, 9722–9731.

4 M. E. Ahmed, R. J. Staples, T. R. Cundari and T. H. Warren, Electrocatalytic Ammonia Oxidation by Pyridyl-Substituted Ferrocenes, *J. Am. Chem. Soc.*, 2025, **144**, 6514–6522.

5 S. Bose, Y. Xia and R. N. Zare, Understanding the formation of nitrate from nitrogen at the interface of gas-water microbubbles, *Chem. Sci.*, 2024, **15**, 19764–19769.

6 H. Y. Liu, H. M. C. Lant, J. L. Troiano, G. Hu, B. Q. Mercado, R. H. Crabtree and G. W. Brudvig, Electrocatalytic, Homogeneous Ammonia Oxidation in Water to Nitrate and Nitrite with a Copper Complex, *J. Am. Chem. Soc.*, 2022, **144**, 8449–8453.

7 S. He, Y. Chen, M. Wang, H. Nuomin, P. Novello, X. Li, S. Zhu and J. Liu, Metal nitride nanosheets enable highly efficient electrochemical oxidation of ammonia, *Nano Energy*, 2021, **80**, 105528.

8 L. Tian, P. Chen, X. H. Jiang, L. S. Chen, L. L. Tong, H. Y. Yang, J. P. Fan, D. S. Wu, J. P. Zou and S. L. Luo, Mineralization of cyanides via a novel Electro-Fenton system generating •OH and •$O_2^-$, *Water Res.*, 2022, **209**, 117890.

9  Q. Jiang, D. M. Xia, X. F. Li, H. Zhang, R. J. Yin, H. J. Xie, H. B. Xie, J. Jiang, J. W. Chen and J. S. Francisco, Rapid $N_2O$ formation from $N_2$ on water droplet surfaces, *Angew. Chem., Int. Ed.*, 2025, **64**, e202421002.

10  F. Habibzadeh, S. L. Miller, T. W. Hamann and M. R. Smith, Homogeneous electrocatalytic oxidation of ammonia to $N_2$ under mild conditions, *Proc. Natl. Acad. Sci. U. S. A.*, 2019, **116**, 2849–2853.

11  L. Tian, M. Y. Yin, L. L. Zheng, Y. Chen, W. Liu, J. P. Fan, D. S. Wu, J. P. Zou and S. L. Luo, Extremely efficient mineralizing CN⁻ into $N_2$ via a newly developed system of generating sufficient $ClO\bullet/Cl_2^{\bullet-}$ and self-decreasing pH, *Sep. Purif. Technol.*, 2023, **309**, 123021.

12  S. I. Venturini, D. R. Martins De Godoi and J. Perez, Challenges in Electrocatalysis of Ammonia Oxidation on Platinum Surfaces: Discovering Reaction Pathways, *ACS Catal.*, 2023, **13**, 10835–10845.

13  Y. Li, H. S. Pillai, T. Wang, S. Hwang, Y. Zhao, Z. Qiao, Q. Mu, S. Karakalos, M. Chen, J. Yang, D. Su, H. Xin, Y. Yan and G. Wu, High-performance ammonia oxidation catalysts for anion-exchange membrane direct ammonia fuel cells, *Energy Environ. Sci.*, 2021, **14**, 1449–1460.

14  F. Fang, Q. Y. Cheng, M. F. Wang, Y. Z. He, Y. F. Huan, S. S. Liu, T. Qian, C. L. Yan and J. M. Lu, Identifying Upper d-Band Edge as Activity Descriptor for Ammonia Oxidation on PtCo Alloys in Low-Temperature Direct Ammonia Fuel Cells, *ACS Nano*, 2025, **19**, 1260–1270.

15  L. Tian, X. Y. Xia, L. J. Zhou, L. L. Zheng, Q. J. Xing, L. S. Zhang, J. P. Zou and Z. Q. Liu, Enhanced chlorine enrichment via electron-deficient centers of Co(III) for efficient electrochlorination and ammonia removal, *Appl. Catal., B*, 2024, **340**, 123260.

16  Z. P. Yu, G. J. Xia, V. M. Diaconescu, L. Simonelli, A. P. LaGrow, Z. X. Tai, X. Y. Xiang, D. H. Xiong and L. F. Liu, Atomically dispersed dinuclear iridium active sites for efficient and stable electrocatalytic chlorine evolution reaction, *Chem. Sci.*, 2024, **15**, 9216–9223.

17  J. Z. He, C. Zhang, Y. Yang, J. W. Kang, C. Y. Zhang, D. He and J. X. Ma, Chlorine-Mediated Ammonia and Organics Transformation during Electrochemical Ammonia Recovery from Human Urine, *Environ. Sci. Technol.*, 2025, **59**, 13096–13107.

18  H. G. Oswin and M. Salomon, The anodic oxidation of ammonia at platinum black electrodes in aqueous KOH electrolyte, *Can. J. Chem.*, 1963, **41**, 1686–1694.

19  H. Y. Liu, H. M. C. Lant, C. Decavoli, R. H. Crabtree and G. W. Brudvig, pH-Dependent Electrocatalytic Aqueous Ammonia Oxidation to Nitrite and Nitrate by a Copper(II) Complex with an Oxidation-Resistant Ligand, *J. Am. Chem. Soc.*, 2025, **147**, 1624–1630.

20  G. Chen, X. L. Ding, P. He, T. Cheng, Y. Chen, J. Lin, X. Zhang, S. Zhao, N. Qiao and X. Y. Yi, Understanding the factors governing the ammonia oxidation reaction by a mononuclear ruthenium complex, *Chem. Sci.*, 2025, **16**, 7573–7578.

21  M. Anand, C. S. Abraham and J. K. Nørskov, Electrochemical oxidation of molecular nitrogen to nitric acid -towards a molecular level understanding of the challenges, *Chem. Sci.*, 2021, **12**, 6442–6448.

22  H. Gerischer and A. Mauerer, Untersuchungen Zur anodischen Oxidation von Ammoniak an Platin-Elektroden, *J. Electroanal. Chem. Interfacial Electrochem.*, 1970, **25**, 421–433.

23  K. Yang, J. Liu and B. Yang, Mechanism and Active Species in $NH_3$ Dehydrogenation under an Electrochemical Environment: An *Ab initio* Molecular Dynamics Study, *ACS Catal.*, 2021, **11**, 4310–4318.

24  X. Chen, Z. Y. Ke, X. Wang, H. Q. Jin, Y. W. Cheng, Y. K. Xiao, R. Jiang, Y. M. Da, L. Fan, H. X. Li, D. M. Liu, S. F. Yang and W. Chen, Fullerene Network-Buffered Platinum Nanoparticles Toward Efficient and Stable Electrochemical Ammonia Oxidation Reaction for Hydrogen Production, *Angew. Chem., Int. Ed.*, 2025, **137**, e202505180.

25  G. L. Li, Y. H. Shi, R. Y. Huang, T. G. Ma, Q. Zhuo, L. Xu, F. Jiang, Y. K. Zhai, Y. H. Xiao, Y. Yan and Y. Zhao, An ingenious structural design of NiCu-MOF bar-like nanosheet array: harnessing synergistic effects to attain exceptional ammonia oxidation performance, *Chem. Eng. J.*, 2025, **521**, 166548.

26  X. Yang, L. Sun, X. Liu, Z. Yang, H. Sun, W. Liu and H. Chen, Vacancy-driven ammonia electrooxidation reaction on the nanosized $CeO_x$ electrode in nonaqueous electrolyte, *ACS Catal.*, 2024, **14**, 6236–6246.

27  H. Y. Fu, F. C. Gu, Y. Z. Niu, S. X. Liao, Z. Y. Bu, H. N. Wang, D. Yang, X. S. Wang and Q. Li, Spatially confined transition metals boost high initial coulombic efficiency in alloy anodes, *Chem. Sci.*, 2025, **16**, 418–424.

28  D. Sun, X. Hong, K. Wu, K. S. Hui, Y. Du and K. N. Hui, Simultaneous removal of ammonia and phosphate by electro-oxidation and electrocoagulation using $RuO_2$-$IrO_2$/Ti and microscale zero-valent iron composite electrode, *Water Res.*, 2020, **169**, 115239.

29  C. X. Liu, Z. F. Teng, X. Liu, R. Zhang, J. Q. Chi, J. W. Zhu, J. F. Qin, X. B. Liu, Z. X. Wu and L. Wang, Stabilizing NiFe active sites using a high-valent Lewis acid for selective seawater oxidation, *Chem. Sci.*, 2025, **16**, 16321–16330.

30  F. Chang, W. Gao, J. Guo and P. Chen, Emerging Materials and Methods toward Ammonia-Based Energy Storage and Conversion, *Adv. Mater.*, 2021, **33**, 2005721.

31  Z. Hu, S. Lu, F. Tang, D. Yang, C. Zhang, Q. Xiao and P. Ming, High-performance precious metal-free direct ammonia fuel cells endowed by Co-doped $Ni_4Cu_1$ anode catalysts, *Appl. Catal., B*, 2023, **334**, 122856.

32  H. Zhong, Q. Zhang, J. Yu, X. Zhang, C. Wu, Y. Ma, H. An, H. Wang, J. Zhang, X. Wang and J. Xue, Fundamental Understanding of Structural Reconstruction Behaviors in Oxygen Evolution Reaction Electrocatalysts, *Adv. Energy Mater.*, 2023, **13**, 2301391.

33  X. Jiang, D. Ying, X. Liu, M. Liu, S. Zhou, C. Guo, G. Zhao, Y. Wang and J. Jia, Identification of the role of Cu site in Ni-Cu hydroxide for robust and high selective electrochemical ammonia oxidation to nitrite, *Electrochim. Acta*, 2020, **345**, 136157.

34 J. J. Medvedev, Y. Tobolovskaya, X. V. Medvedeva, S. W. Tatarchuk, F. Li and A. Klinkova, Pathways of ammonia electrooxidation on nickel hydroxide anodes and an alternative route towards recycled fertilizers, *Green Chem.*, 2022, **24**, 1578–1589.

35 APHA, AWWA and WEF, *Standard Methods for the Examination of Water and Wastewater*, APHA, Washington, DC, 22th edn, 2012.

36 M. Pandurangappa and Y. Venkataramanappa, Aminophenyl Benzimidazole as a New Reagent for the Estimation of $NO_2$/Nitrite/Nitrate at Trace Level: Application to Environmental Samples, *Anal. Lett.*, 2007, **40**, 2974–2991.

37 W. J. Duan, G. Li, Z. C. Lei, T. G. Zhu, Y. Z. Xue, C. H. Wei and C. H. Feng, Highly active and durable carbon electrocatalyst for nitrate reduction reaction, *Water Res.*, 2019, **161**, 126–135.

38 Y. H. Wang, F. Y. Gao, X. L. Zhang, Y. Yang, J. Liao, Z. Z. Niu, S. Qin, P. P. Yang, P. C. Yu, M. Sun and M. R. Gao, Efficient $NH_3$-Tolerant Nickel-Based Hydrogen Oxidation Catalyst for Anion Exchange Membrane Fuel Cells, *J. Am. Chem. Soc.*, 2023, **145**, 17485–17494.

39 M. Zhu, Y. Yang, S. Xi, C. Diao, Z. Yu, W. S. V. Lee and J. Xue, Deciphering $NH_3$ Adsorption Kinetics in Ternary Ni-Cu-Fe Oxyhydroxide toward Efficient Ammonia Oxidation Reaction, *Small*, 2021, **17**, 2005616.

40 N. Yao, G. Wang, H. Jia, J. Yin, H. Cong, S. Chen and W. Luo, Intermolecular Energy Gap-Induced Formation of High-Valent Cobalt Species in CoOOH Surface Layer on Cobalt Sulfides for Efficient Water Oxidation, *Angew. Chem., Int. Ed.*, 2022, **61**, e202117178.

41 Z. Zhou, Y. Xie, L. Sun, Z. Wang, W. Wang, L. Jiang, X. Tao, L. Li, X. H. Li and G. Zhao, Strain-induced in situ formation of NiOOH species on Co-Co bond for selective electrooxidation of 5-hydroxymethylfurfural and efficient hydrogen production, *Appl. Catal., B*, 2022, **305**, 121072.

42 L. Y. Hao, Z. J. Tang, C. Y. Cai, Y. C. Zhao, L. Tian, N. Li and Z. Q. Liu, Electron-delocalized $Cu^{2+}$ activates spin channels in spinel oxides to selectively produce $^1O_2$ for wastewater treatment, *Angew. Chem., Int. Ed.*, 2025, **64**, e202504426.

43 L. Tian, L. Zhang, L. Zheng, Y. Chen, L. Ding, J. Fan, D. Wu, J. Zou and S. Luo, Overcoming Electrostatic Interaction via Strong Complexation for Highly Selective Reduction of $CN^-$ into $N_2$, *Angew. Chem., Int. Ed.*, 2022, **61**, e202214145.

44 J. J. Liang, C. Y. Du, Y. J. Xian, C. Y. Cai, L. Tian, Y. H. Ao, P. F. Wang and Z. Q. Liu, Accelerating *OH desorption via electron-delocalized $Cu_{Td}^{2+}$-O-$Co_{Oh}^{3+}$ for water purification, *Adv. Funct. Mater.*, 2025, **35**, 2503514.

45 L. Tian, Z. J. Tang, L. Y. Hao, T. Dai, J. P. Zou and Z. Q. Liu, Efficient homolytic cleavage of $H_2O_2$ on hydroxyl-enriched spinel $CuFe_2O_4$ with dual Lewis acid sites, *Angew. Chem., Int. Ed.*, 2024, **63**, e202401434.

46 V. T. T. Phan, Q. P. Nguyen, B. Wang and I. J. Burgess, Oxygen Vacancies Alter Methanol Oxidation Pathways on NiOOH, *J. Am. Chem. Soc.*, 2024, **146**, 4830–4841.

47 Z. Tian, M. Wang, G. Chen, J. Chen, Y. Da, H. Zhang, R. Jiang, Y. Xiao, B. Cui, C. Jiang, Y. Ding, J. Yang, Z. Sun, C. Han and W. Chen, n-$ZrS_3$/p-ZrOS Photoanodes with NiOOH/FeOOH Oxygen Evolution Catalysts for Photoelectrochemical Water Oxidation, *Angew. Chem., Int. Ed.*, 2024, e202414209.

48 M. Gonzalez-Reyna, M. S. Luna-Martínez and J. F. Perez-Robles, Nickel supported on carbon nanotubes and carbon nanospheres for ammonia oxidation reaction, *Nanotechnology*, 2020, **31**, 235706.

49 J. Yao, M. Zhou, D. Wen, Q. Xue and J. Wang, Electrochemical conversion of ammonia to nitrogen in non-chlorinated aqueous solution by controlling pH value, *J. Electroanal. Chem.*, 2016, **776**, 53–58.

50 J. Song, Y. Yinhai, Y. Jia, T. Wang, J. Wei, M. Wang, S. Zhou, Z. Li, Y. Hou, L. Lei and B. Yang, Improved $NH_3$-N conversion efficiency to $N_2$ activated by BDD substrate on NiCu electrocatalysis process, *Sep. Purif. Technol.*, 2021, **276**, 119350.

51 Y. J. Shih and C. H. Hsu, Kinetics and highly selective $N_2$ conversion of direct electrochemical ammonia oxidation in an undivided cell using NiCo oxide nanoparticle as the anode and metallic Cu/Ni foam as the cathode, *Chem. Eng. J.*, 2021, **409**, 128024.

52 R. Wang, H. Liu, K. Zhang, G. Zhang, H. Lan and J. Qu, Ni(II)/Ni(III) redox couple endows Ni foam-supported $Ni_2P$ with excellent capability for direct ammonia oxidation, *Chem. Eng. J.*, 2021, **404**, 126795.

53 S. S. P. Rahardjo and Y. J. Shih, Electrochemical characteristics of silver/nickel oxide (Ag/Ni) for direct ammonia oxidation and nitrogen selectivity in paired electrode system, *Chem. Eng. J.*, 2023, **452**, 139370.

54 Y. J. Shih, Y. H. Huang and C. P. Huang, Electrocatalytic ammonia oxidation over a nickel foam electrode: role of $Ni(OH)_{2(s)}$-$NiOOH_{(s)}$ nanocatalysts, *Electrochim. Acta*, 2018, **263**, 261–271.

55 P. Zhou, S. Zhang, Z. Ren, X. Tang, K. Zhang, R. Zhou, D. Wu, J. Liao, Y. Zhang and C. Huang, In Situ Cutting of Ammonium Perchlorate Particles by Co-Bipy "scalpel" for High Efficiency Thermal Decomposition, *Adv. Sci.*, 2022, **9**, 2204109.

56 Y. Peng, W. Si, X. Li, J. Chen, J. Li, J. Crittenden and J. Hao, Investigation of the Poisoning Mechanism of Lead on the $CeO_2$-$WO_3$ Catalyst for the $NH_3$-SCR Reaction via in Situ IR and Raman Spectroscopy Measurement, *Environ. Sci. Technol.*, 2016, **50**, 9576–9582.

57 R. M. S. Yoo, D. Yesudoss, D. Johnson and A. Djire, A Review on the Application of In-situ Raman Spectroelectrochemistry to Understand the Mechanisms of Hydrogen Evolution Reaction, *ACS Catal.*, 2023, **13**, 10570–10601.

58 L. Bai, F. Franco, J. Timoshenko, C. Rettenmaier, F. Scholten, H. S. Jeon, A. Yoon, M. Rüscher, A. Herzog, F. T. Haase, S. Kühl, S. W. Chee, A. Bergmann and R. C. Beatriz, Electrocatalytic Nitrate and Nitrite Reduction toward Ammonia Using $Cu_2O$ Nanocubes: Active Species and Reaction Mechanisms, *J. Am. Chem. Soc.*, 2024, **146**, 9665–9678.

59 H. Chen, H. Ze, M. Yue, D. Wei, Y. A, Y. Wu, J. Dong, Y. Zhang, H. Zhang, Z. Tian and J. Li, Unmasking the Critical Role of the Ordering Degree of Bimetallic Nanocatalysts on Oxygen Reduction Reaction by In situ Raman Spectroscopy, *Angew. Chem., Int. Ed.*, 2022, **134**, e202117834.